LETTER

doi:10.1038/nature23674

A spin transition mechanism for cooperative adsorption in metal–organic frameworks

Douglas A. Reed[1]*, Benjamin K. Keitz[1,2]*, Julia Oktawiec[1], Jarad A. Mason[1], Tomče Runčevski[1,3], Dianne J. Xiao[1], Lucy E. Darago[1], Valentina Crocellà[4], Silvia Bordiga[4] & Jeffrey R. Long[1,3,5]

Cooperative binding, whereby an initial binding event facilitates the uptake of additional substrate molecules, is common in biological systems such as haemoglobin[1,2]. It was recently shown that porous solids that exhibit cooperative binding have substantial energetic benefits over traditional adsorbents[3], but few guidelines currently exist for the design of such materials. In principle, metal–organic frameworks that contain coordinatively unsaturated metal centres could act as both selective[4–7] and cooperative adsorbents if guest binding at one site were to trigger an electronic transformation that subsequently altered the binding properties at neighbouring metal sites[8–10]. Here we illustrate this concept through the selective adsorption of carbon monoxide (CO) in a series of metal–organic frameworks featuring coordinatively unsaturated iron(II) sites. Functioning via a mechanism by which neighbouring iron(II) sites undergo a spin-state transition above a threshold CO pressure, these materials exhibit large CO separation capacities with only small changes in temperature. The very low regeneration energies that result may enable more efficient Fischer–Tropsch conversions and extraction of CO from industrial waste feeds, which currently underutilize this versatile carbon synthon[11]. The electronic basis for the cooperative adsorption demonstrated here could provide a general strategy for designing efficient and selective adsorbents suitable for various separations.

Metal–organic frameworks are highly porous, chemically tunable solids that have been investigated as selective adsorbents for gas separation applications[12–14]. These systems typically exhibit classical, type I adsorption isotherms (Fig. 1a). However, a trade-off between selectivity and working capacity is encountered, as steeper isotherms are generally associated with greater selectivity but consequently require harsher regeneration conditions. A more energetically favourable separation method involves cooperative adsorption, wherein little adsorption is observed until a sharp rise, or step, occurs, where the majority of gas is adsorbed over a narrow pressure region (Fig. 1b). Owing to the temperature dependence of the step pressure, such adsorbents combine high working capacities with modest temperature swings, as moving the step between the adsorption and desorption pressures recovers large quantities of adsorbed gas.

Although step-shaped isotherms are well established, the vast majority occur in pressure-responsive flexible frameworks[15,16] or arise when adsorbate–adsorbate interactions become important[17]. Although useful for other applications, the responsive nature of these systems does not contribute substantially to selective gas adsorption. Thus far, the only reported mechanism for selective cooperative adsorption in rigid metal–organic frameworks involves rearrangement of amines to form ammonium carbamate chains upon CO_2 adsorption[3]. However, this mechanism is specific to CO_2, and designing cooperative adsorbents for other industrially relevant gases requires a different strategy.

In nature, cooperative binding is accomplished by transition metals in enzymes, with an initial binding event inducing an electronic response at the active site and a corresponding structural change throughout the system. This promotes subsequent substrate binding at neighbouring active sites, as observed with O_2 or CO uptake in haemoglobin[1,2]. Metal–organic frameworks that feature coordinatively unsaturated metal sites have been studied for applications involving selective gaseous substrate binding[4–7], but these adsorption sites are often treated as isolated centres that operate independently from one another. With an appropriate design, the electronic properties of a transition metal situated within an extended network can influence the binding properties of neighbouring metal sites[8–10]. By combining these strategies, a framework that contains coordinatively unsaturated metal sites that are closely linked, such that electronic properties change in a concerted fashion upon gas binding, might be expected to behave as a cooperative and selective adsorbent, mimicking the cooperative electronic and subsequent structural transitions observed in biological systems.

We selected carbon monoxide (CO) as a sorbate to test this hypothesis because, as the quintessential strong-field ligand, its coordination induces spin transitions in otherwise high-spin molecular species[18]. Spin transitions are highly dependent on the proximity of neighbouring spin transition centres[8,9], and provide an appropriate electronic transformation for potential cooperative adsorption. In addition, industrial CO separations are widely implemented, and a selective and easily regenerable CO adsorbent would be immediately applicable[11]. A triazolate-based metal–organic framework was recently reported with iron(II) centres that selectively convert from a high-spin to a low-spin electron configuration upon CO coordination[19]. However, no cooperative phase transition was observed owing to the large distance between the tetranuclear iron nodes. We envisioned that a structure wherein iron(II) sites with a similar coordination environment were linked into chains would create a favourable environment for a cooperative spin transition upon CO adsorption. Here we report two such metal–organic frameworks, Fe_2Cl_2(bbta) (**1**; H_2bbta = 1*H*,5*H*-benzo(1,2-*d*:4,5-*d*′)bistriazole) and Fe_2Cl_2(btdd) (**2**; H_2btdd = bis(1*H*-1,2,3-triazolo[4,5-*b*],[4′,5′-*i*])dibenzo[1,4]dioxin), which indeed adsorb CO through a cooperative spin transition mechanism. This mechanism results in highly efficient CO separations and demonstrates that rational design of cooperative adsorbents can be achieved by controlling the electronic properties at open metal sites.

We synthesized microcrystalline powders of **1** and **2**, and powder X-ray diffraction data show both materials to be isostructural to previously reported analogues[20–22]. In the desolvated forms of these compounds, helical chains of square pyramidal iron(II) centres, each ligated by three triazolates and two chlorides, are linked into a highly porous three-dimensional framework that features a hexagonal array

[1]Department of Chemistry, University of California, Berkeley, California 94720, USA. [2]McKetta Department of Chemical Engineering, University of Texas, Austin, Texas 78712, USA. [3]Materials Sciences Division, Lawrence Berkeley National Laboratory, Berkeley, California 94720, USA. [4]Chemistry Department, NIS and INSTM Centre of Reference, University of Turin, Via Quarello 15, I-10135 Torino, Italy. [5]Department of Chemical and Biomolecular Engineering, University of California, Berkeley, California 94720, USA.
*These authors contributed equally to this work.

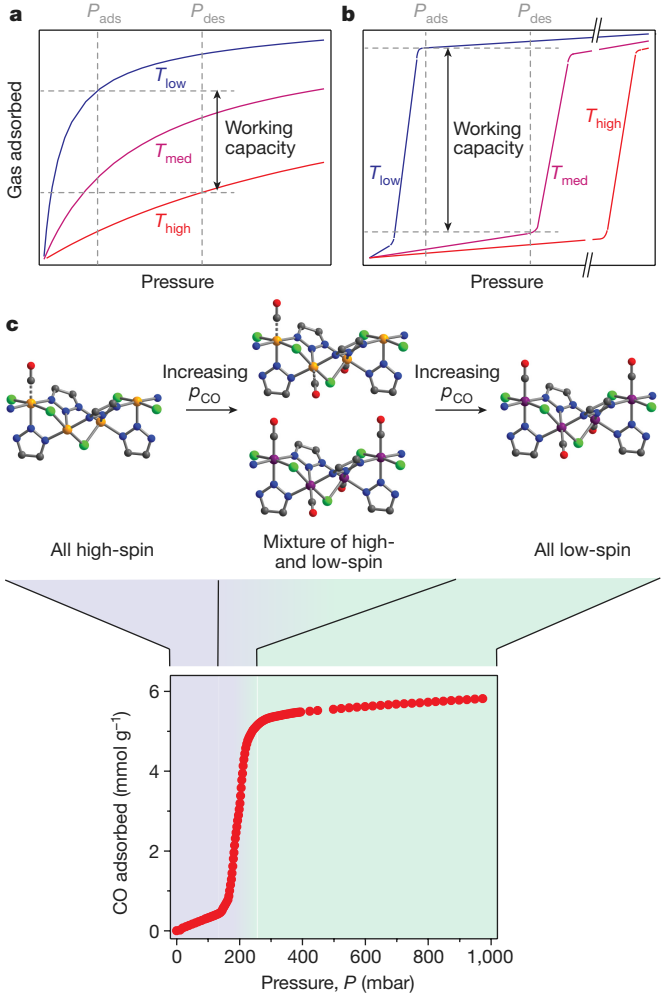

Figure 1 | Idealized adsorption isotherms and the cooperative spin transition mechanism. a, **b**, Comparison of working capacities for idealized gas adsorption isotherms of classical (**a**) and cooperative (**b**) adsorbents, highlighting the increased working capacity for a cooperative adsorbent using a smaller temperature swing (T_{low} to T_{med} instead of T_{low} to T_{high}, for the same P_{ads} and P_{des}). P_{ads} and P_{des} are the adsorption and desorption pressures; T_{low}, T_{med} and T_{high} are representative low, medium and high temperatures. **c**, Schematic of the cooperative spin transition mechanism. At a CO partial pressure p_{CO} below the step region of the isotherm, a phase consisting of all high-spin iron(II) (orange spheres) is observed. As the pressure is increased through the step pressure, some high-spin iron(II) is converted to low-spin iron(II) (purple spheres). With further increases in CO pressure, beyond the step pressure, full conversion to a low-spin phase is observed. The relevant regions are indicated on the CO adsorption isotherm of **1** obtained at 25 °C as a function of pressure, *P*. Grey, green, orange, purple, blue and red spheres represent C, Cl, high-spin iron(II), low-spin iron(II), N and O atoms, respectively; H atoms are omitted for clarity.

of one-dimensional channels (Fig. 2). Neighbouring iron sites along the chains are 3.361(5) Å apart in **1** and 3.602(7) Å apart in **2**, and are tightly interconnected, with each chloride and triazolate moiety bridging two and three separate iron sites, respectively.

The structure of the iron(II)–triazolate chains in **1** suggests that the coordination environment of one metal site will be highly sensitive to electronically induced structural changes at adjacent sites. Indeed, the CO adsorption isotherm of **1** collected at 25 °C has a prominent step, with a sharp rise occurring at 170 mbar (Fig. 1c). Analysis of the isotherm data resulted in a Hill coefficient of 10.7 during the transition, suggesting a high degree of cooperativity (Supplementary Fig. 17). The bound CO is readily released in a similar step-shaped isotherm upon decreasing CO pressure, with a hysteresis width of approximately 120 mbar (Supplementary Fig. 11), and complete regeneration of the material is observed over successive adsorption/desorption cycles (Supplementary Fig. 15).

To investigate the mechanism for the unusual adsorption of CO, we analysed powder X-ray diffraction data for activated and CO-dosed samples of **1**. Unlike most materials that have step-shaped isotherms, in which unit cell expansions are observed upon gas loading owing to a gate-opening mechanism[15,16], adsorption of CO causes substantial structural contractions in **1** (Fig. 3). Whereas the activated material has Fe–N and Fe–Cl bond lengths of 2.11(2) Å and 2.385(6) Å, respectively, the CO-bound material (**1**·2CO) has contracted Fe–N and Fe–Cl bond distances of 1.972(5) Å and 2.259(4) Å, respectively. These changes in bond length are consistent with a conversion from high-spin to low-spin iron(II)[18,23]. The assignment of low-spin iron(II) in **1**·2CO is further supported by a Fe–C_{CO} bond length of 1.76(4) Å and a nearly linear Fe–C–O bond angle[18].

Remarkably, *in situ* powder X-ray diffraction studies performed on **1** revealed no detectable intermediates between the high- and low-spin phases, suggesting that the spin transition, once triggered, occurs simultaneously and cooperatively throughout an entire crystallite. A sample of **1** sealed under 300 mbar of CO was subjected to repeated heating and cooling cycles (Fig. 3b). Above 52 °C, even in the presence of CO, we observed a single phase corresponding to all high-spin iron(II). Cooling resulted in the appearance of a distinct new phase with a smaller unit-cell volume, corresponding to the low-spin, CO-bound iron phase. By 25 °C, the conversion to low-spin was complete, as expected from the adsorption data.

Mössbauer spectra and d.c. magnetic susceptibility measurements corroborate the iron(II) spin transition from high to low spin ($S = 2$ to $S = 0$). The Mössbauer spectrum of **1** obtained at 100 K showed one dominant iron site (Supplementary Fig. 19), with an isomer shift of $\delta = 1.084(2)$ mm s^{-1} and a quadrupole splitting of $\Delta E_Q = 1.928(6)$ mm s^{-1}, typical of square pyramidal high-spin iron(II) species[18,23]. Upon *ex situ* dosing of CO, data collection at 100 K revealed a different species, with $\delta = 0.364(2)$ mm s^{-1} and $\Delta E_Q = 0.989(4)$ mm s^{-1}, consistent with low-spin iron(II). Before dosing with CO, we determined the molar magnetic susceptibility (χ_M) times temperature (T), $\chi_M T$, at 300 K to be 3.45 emu K per mol Fe, consistent with all high-spin iron(II). After dosing with CO, this value was greatly diminished, reaching only 0.6 emu K per mol Fe at 300 K (Supplementary Fig. 20). This result again corroborates the spin transition from $S = 2$ to $S = 0$, with the slight residual magnetic moment attributed to incomplete saturation of CO during the experiment.

Infrared spectroscopy was used to probe the nature of the adsorbed CO in **1** at all pressures, including before the adsorption step (Fig. 3c). Below 150 mbar, weakly bound CO with a stretching frequency of $\nu_{CO} = 2{,}157$ cm^{-1} was observed. Compared to free CO, for which $\nu_{CO} = 2{,}143$ cm^{-1}, this blueshifted resonance is attributed to high-spin iron(II)–CO adducts[24]. Upon increasing the pressure past the expected step pressure of 170 mbar, new peaks appear at 2,048 cm^{-1} and 2,039 cm^{-1}, which closely match previously reported values for low-spin iron(II)–CO species[19]. These peaks quickly increase in intensity with increasing CO pressure, suggesting that the majority of the adsorbed CO is bound to low-spin iron(II) after the step.

Combining the structural, magnetic and spectroscopic studies, we propose the following mechanism for the step-shaped CO adsorption isotherm. The proximity and interconnectedness of the iron(II) sites in **1** creates a barrier to the structural rearrangements that are required for the spin-state conversion of a single iron centre. Therefore, at low pressures of CO, the spin state of an individual iron site cannot convert and remains high-spin. However, once a threshold pressure of CO is reached, the transition becomes favourable, at which point all of the iron sites in a crystallite simultaneously convert to the low-spin state. This behaviour is reminiscent of the pressure-induced phase transformations that are observed in flexible materials[15,16], but involves a specific adsorbate-induced electronic response at an open metal site.

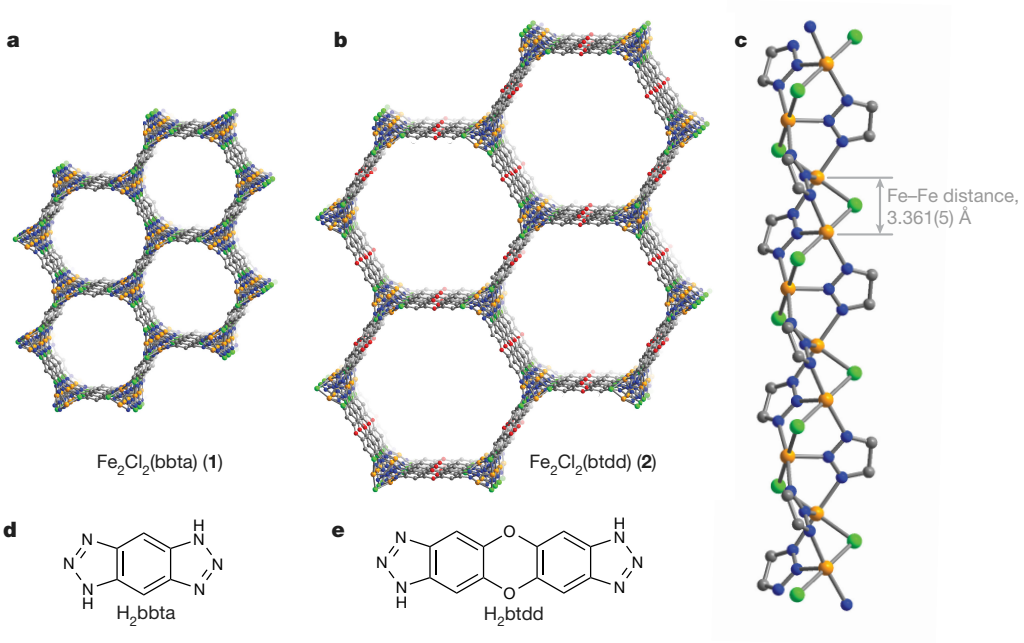

Figure 2 | Solid state structures. a, **b**, Portions of the structures of **1** (**a**) and **2** (**b**) determined from analysis of powder X-ray diffraction data, showing the hexagonal array of one-dimensional channels lined with a high concentration of coordinatively unsaturated iron(II) sites. **c**, Structure of a helical iron–chloride–triazolate chain running along the *c* axis in **1**, with the proximity of adjacent iron centres highlighted. The number in parentheses is the estimated standard deviation in the final digit of the Fe–Fe distance. **d**, **e**, Structures of the linker precursors H_2bbta for **1** (**d**) and H_2btdd for **2** (**e**). Grey, green, orange, blue and red spheres represent C, Cl, Fe, N and O atoms, respectively; H atoms are omitted for clarity.

This design allows **1** to behave similarly to responsive adsorbents in biological systems.

Having confirmed the cooperative nature of the spin transition and CO adsorption, we compared the working capacities, regeneration energies and selectivities of **1** with other leading materials for CO separations. In an industrial context, CO is an intermediate in the conversion of natural gas, biomass and other carbon feedstocks into valuable products, typically through the Fischer–Tropsch process[11]. However, adjusting the H_2:CO ratio in syngas produced from various sources and for every product is energetically costly. Other sources of CO, such as that produced during steel production or coal gasification, are contaminated with N_2, CO_2 and hydrocarbons. These vast resources are usually wasted, and in many instances are burned, accounting for a large portion of the 2.5 Gt of CO_2 produced annually from iron and steel production[25]. Current CO separations generally use energetically costly cryogenic distillation, and liquid- or membrane-based adsorption processes have not been widely implemented[26]. Porous materials, including metal–organic frameworks, have been investigated for CO separations, but face selectivity issues or need improvements in working capacity[19,24,27,28].

Adsorption isotherms obtained at multiple temperatures show that the step pressure of **1** has a pronounced temperature dependence (Fig. 4a).

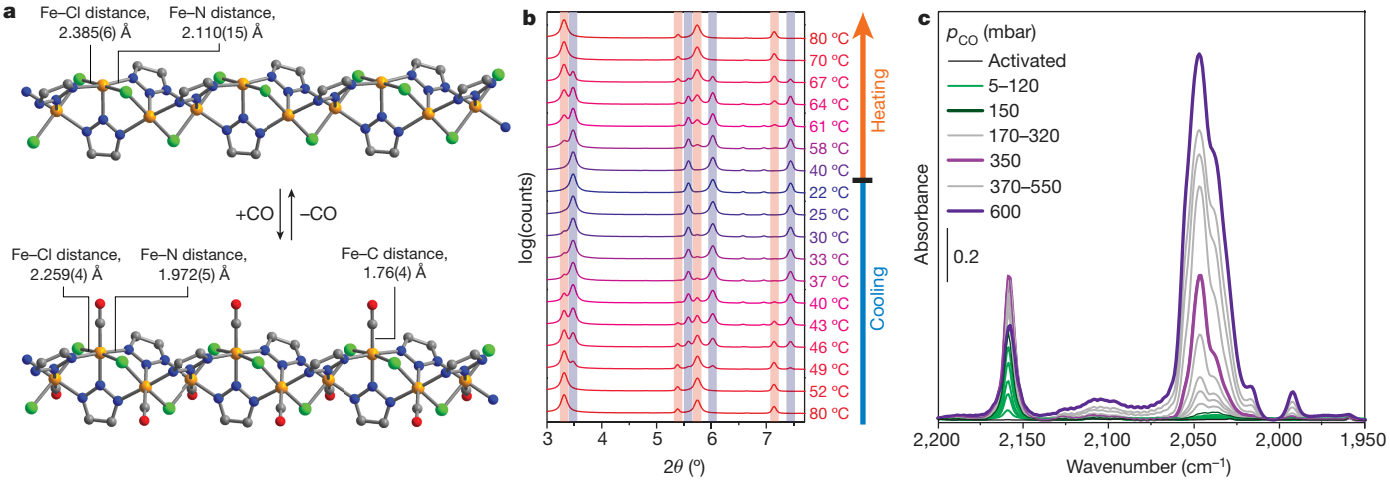

Figure 3 | Characterization of the spin transition mechanism. a, Portions of the structures of **1** (upper) and **1**·2CO (lower), with selected bond lengths indicated. Grey, green, orange, blue and red spheres represent C, Cl, Fe, N and O atoms, respectively; H atoms are omitted for clarity. Numbers in parentheses are the estimated standard deviation in the final digit of each number. **b**, Powder X-ray diffraction data for **1** under 300 mbar of CO obtained at various temperatures (as indicated) with a wavelength of 0.72768 Å. Peaks corresponding to the high-spin phase are shaded in red and peaks corresponding to the low-spin, CO-bound phase are shaded in blue. The spectra are offset for clarity. **c**, Infrared spectra of **1** obtained at 25 °C at various partial pressures of CO (p_{CO}). All spectra are shown as the difference with respect to the spectrum of the activated sample, with the gas-phase CO spectra subtracted.

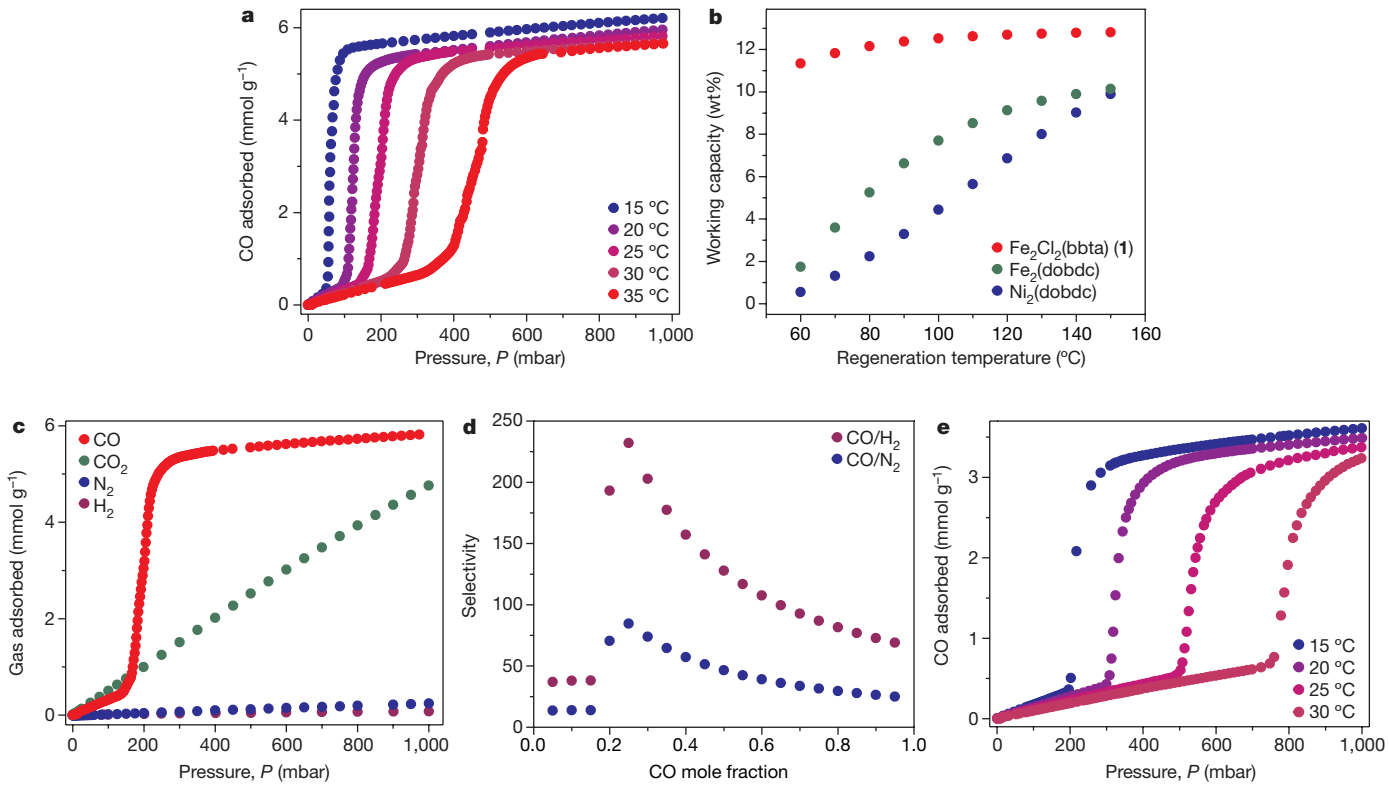

Figure 4 | Gas adsorption isotherms, working capacities, and molar selectivity values. a, Adsorption isotherms of CO obtained for **1** at selected temperatures. **b**, Comparison of CO separation working capacities for **1** with those calculated for the classical CO adsorbents Fe_2(dobdc) and Ni_2(dobdc) (dobdc^{4-} = 2,5-dioxido-1,4-benzenedicarboxylate), with adsorption at 0.2 bar and 20 °C and desorption at 1.0 bar and the specified regeneration temperatures. **c**, Single-component adsorption isotherms of CO, CO_2, N_2 and H_2 for **1** obtained at 25 °C. **d**, Molar selectivity for mixtures of CO and selected gases (N_2 or H_2) at varying concentrations for 25 °C and 1.0 bar of total pressure in **1**, with the step position occurring at a CO mole fraction of approximately 0.2. **e**, Adsorption isotherms of CO obtained for **2** at selected temperatures, highlighting the differences in the adsorption properties compared to **1** (**a**), caused by the different ligand environments of the iron(II) centres.

A change in temperature of only 5 °C (25 °C to 30 °C) results in an 80-mbar increase in step pressure (Supplementary Fig. 11), and similar shifts occur in the desorption isotherms. Standard temperature swing adsorption processes should recover nearly all of the CO adsorbed without the need for a purge gas if the desorption step pressure is above 1 bar, which occurs near 60 °C in **1**. As an example of a working process, adsorption at 200 mbar and 20 °C and desorption at 1 bar and 60 °C (a temperature swing of only 40 °C) corresponds to a CO removal capacity of 11.4 wt%. This is a much greater working capacity than has been achieved using the best non-cooperative adsorbents, which are estimated to require temperature swings in excess of 100 °C to achieve comparable working capacities[24] (Fig. 4b). Notably, unlike classical adsorbents, **1** only requires the step position to be lower than the CO partial pressure to achieve these high working capacities, so higher adsorption temperatures can be used in gas mixtures with higher partial pressures of CO.

The cooperative adsorption mechanism enables highly efficient regeneration of the adsorbent. Using differential scanning calorimetry data to calculate the heat capacities of **1** (Supplementary Fig. 21) and the Clausius–Clapeyron relation to calculate the isosteric heats of CO adsorption (−66 kJ mol^{-1}; Supplementary Fig. 14), regeneration energies as low as 2.66 MJ per kg CO were obtained, with adsorption at 20 °C at 200 mbar and desorption at 60 °C and 1 bar, and without using any purge gas. For comparison, the COSORB process, a leading alternative to cryogenic distillation, requires up to 8.31 MJ per kg CO for regeneration[29].

To test the selectivity of **1** in CO separation applications, we measured the pure-component adsorption isotherms of other gases. At 25 °C, **1** adsorbs much less H_2 and N_2 than CO (Fig. 4c). We calculated the molar selectivity from the pure-component isotherms to be 232 for a 1:3 CO:H_2 ratio at 25 °C and 1.0 bar of total pressure, with similarly high selectivities obtained for CO/N_2 mixtures (Fig. 4d). These high selectivity values demonstrate the utility of **1** for potential CO separations. Unlike most CO adsorbents that feature exposed metal sites, the spin-state transition mechanism enables **1** to bind CO selectively over more polarizable gas molecules[19] such as CO_2. For all pressures above the step pressure, **1** adsorbed more CO than CO_2 and demonstrated a stronger binding enthalpy of −66 kJ mol^{-1} compared to −23 kJ mol^{-1} for CO_2, indicating the potential for selective CO adsorption even in the presence of typically more strongly adsorbing species.

Because spin transitions are highly sensitive to changes in the ligand field of the transition metal[23] and even to subtle outer-sphere changes[30], we hypothesized that simple electronic modifications to the linker could result in substantial changes in the adsorption properties. Therefore, we replaced bbta^{2-} with btdd^{2-} to form the isotypic metal–organic framework **2** (Fig. 2b). This new linker results in subtle electronic differences in the iron environment owing to its ether moieties. Analogous to those observed in **1**, adsorption isotherms of CO in **2** display sharp steps, indicating a similar adsorption mechanism (Fig. 4e). However, the step position at each temperature shifted considerably, from 170 mbar in **1** to 500 mbar in **2** at 25 °C. Other synthetic modifications to the triazolate ligand or to the bridging halide could be used to create systems with different step positions. Such tunability provides a means of customizing materials within this class of cooperative adsorbents, because the position of the adsorption step can be optimized for a given CO separation, dictated by the temperature and partial pressure of CO in a gas mixture. Moreover, by using this tunability to further strengthen the ligand field at the iron(II) centres, it should be possible to realize analogous frameworks that exhibit cooperative adsorption of other key industrial gas molecules, including acetylene, ethylene,

propylene and possibly even dinitrogen. The cooperative spin transition mechanism provides a potentially powerful method for tuning an adsorbent to separate molecules efficiently, and could revolutionize the means by which energy-intensive gas separations are performed.

Online Content Methods, along with any additional Extended Data display items and Source Data, are available in the online version of the paper; references unique to these sections appear only in the online paper.

Received 19 April; accepted 24 July 2017.
Published online 11 September 2017.

1. Perutz, M. F. *Mechanism of Cooperativity and Allosteric Regulation in Proteins* (Cambridge Univ. Press, 1990).
2. Perrella, M. & Di Cera, E. CO ligation intermediates and the mechanism of hemoglobin cooperativity. *J. Biol. Chem.* **274,** 2605–2608 (1999).
3. McDonald, T. M. *et al.* Cooperative insertion of CO_2 in diamine-appended metal-organic frameworks. *Nature* **519,** 303–308 (2015).
4. Caskey, S. R., Wong-Foy, A. G. & Matzger, A. J. Dramatic tuning of carbon dioxide uptake via metal substitution in a coordination polymer with cylindrical pores. *J. Am. Chem. Soc.* **130,** 10870–10871 (2008).
5. Sumida, K. *et al.* Carbon dioxide capture in metal–organic frameworks. *Chem. Rev.* **112,** 724–781 (2012).
6. Herm, Z. R., Bloch, E. D. & Long, J. R. Hydrocarbon separations in metal–organic frameworks. *Chem. Mater.* **26,** 323–338 (2014).
7. Xiao, D. J. *et al.* Selective, tunable O_2 binding in cobalt(II)–triazolate/pyrazolate metal–organic frameworks. *J. Am. Chem. Soc.* **138,** 7161–7170 (2016).
8. Kahn, O. & Martinez, C. J. Spin-transition polymers: from molecular materials toward memory devices. *Science* **279,** 44–48 (1998).
9. Niel, V., Martinez-Agudo, J. M., Munoz, M. C., Gaspar, A. B. & Real, J. A. Cooperative spin crossover behavior in cyanide-bridged Fe(II)–M(II) bimetallic 3D Hofmann-like networks (M = Ni, Pd, Pt). *Inorg. Chem.* **40,** 3838–3839 (2001).
10. Foucher, D. A., Honeyman, C. H., Nelson, J. M., Tang, B. Z. & Manners, I. Organometallic ferrocenyl polymers displaying tunable cooperative interactions between transition metal centers. *Angew. Chem. Int. Edn Engl.* **32,** 1709–1711 (1993).
11. Kerry, F. G. *Industrial Gas Handbook: Gas Separation and Purification* Ch. 8 (CRC, 2007).
12. Zhou, H. C., Long, J. R. & Yaghi, O. M. Introduction to metal–organic frameworks. *Chem. Rev.* **112,** 673–674 (2012).
13. Furukawa, H., Cordova, K. E., O'Keeffe, M. & Yaghi, O. M. The chemistry and applications of metal-organic frameworks. *Science* **341,** 1230444 (2013).
14. Li, J.-R., Kuppler, R. J. & Zhou, H.-C. Selective gas adsorption and separation. *Chem. Soc. Rev.* **38,** 1477–1504 (2009).
15. Schneemann, A. *et al.* Flexible metal–organic frameworks. *Chem. Soc. Rev.* **43,** 6062–6096 (2014).
16. Serre, C. *et al.* An explanation for the very large breathing effect of a metal–organic framework during CO_2 adsorption. *Adv. Mater.* **19,** 2246–2251 (2007).
17. Walton, K. S. *et al.* Understanding inflections and steps in carbon dioxide adsorption isotherms in metal–organic frameworks. *J. Am. Chem. Soc.* **130,** 406–407 (2008).
18. Benito-Garagorri, D., Lagoja, I., Veiros, L. F. & Kirchner, K. A. Reactivity of coordinatively unsaturated iron complexes towards carbon monoxide: to bind or not to bind? *Dalton Trans.* **40,** 4778–4792 (2011).
19. Reed, D. A. *et al.* Reversible CO scavenging via adsorbate-dependent spin state transitions in an iron(II)–triazolate metal–organic framework. *J. Am. Chem. Soc.* **138,** 5594–5602 (2016).
20. Liao, P.-Q. *et al.* Drastic enhancement of catalytic activity via post-oxidation of a porous Mn^{II} triazolate framework. *Chem. Eur. J.* **20,** 11303–11307 (2014).
21. Liao, P.-Q. *et al.* Monodentate hydroxide as a super strong yet reversible active site for CO_2 capture from high-humidity flue gas. *Energy Environ. Sci.* **8,** 1011–1016 (2015).
22. Rieth, A. J., Tulchinsky, Y. & Dincă, M. High and reversible ammonia uptake in mesoporous azolate metal–organic frameworks with open Mn, Co, and Ni sites. *J. Am. Chem. Soc.* **138,** 9401–9404 (2016).
23. Garcia, Y., Niel, V., Munoz, M. C. & Real, J. A. Spin crossover in 1D, 2D, and 3D polymeric Fe(II) networks. *Top. Curr. Chem.* **233,** 229–257 (2004).
24. Bloch, E. D. *et al.* Reversible CO binding enables tunable CO/H_2 and CO/N_2 separations in metal-organic frameworks with exposed divalent metal cations. *J. Am. Chem. Soc.* **136,** 10752–10761 (2014).
25. International Energy Agency. *Global Action to Advance Carbon Capture and Storage: A Focus on Industrial Applications* http://www.iea.org/publications/freepublications/publication/CCS_Annex.pdf (IEA, 2013).
26. Dutta, N. N. & Patil, G. S. Developments in CO separation. *Gas. Sep. Purif.* **9,** 277–283 (1995).
27. Sato, H. *et al.* Self-accelerating CO sorption in a soft nanoporous crystal. *Science* **343,** 167–170 (2014).
28. Peng, J. *et al.* A supported Cu(I)@MIL-100(Fe) adsorbent with high CO adsorption capacity and CO/N_2 selectivity. *Chem. Eng. J.* **270,** 282–289 (2015).
29. Davis, R. A., Nicholas, D. M., Smith, D. D., Wang, S.-I. & Wright, R. A. Integrated reformer process for the production of carbon black. US patent 5,011,670 (1991).
30. Halder, G. J., Kepert, C. J., Moubaraki, B., Murray, K. S. & Cashion, J. D. Guest-dependent spin crossover in a nanoporous molecular framework material. *Science* **298,** 1762–1765 (2002).

Supplementary Information is available in the online version of the paper.

Acknowledgements This research was supported through the Center for Gas Separations Relevant to Clean Energy Technologies, an Energy Frontier Research Center funded by the US Department of Energy, Office of Science, Office of Basic Energy Sciences under award DE-SC0001015. Powder X-ray diffraction data were collected at Beamline 11-BM and Beamline 17-BM at the Advanced Photon Source, a DOE Office of Science User Facility, operated by Argonne National Laboratory under contract DE-AC02-06CH11357. We thank P. C. Bunting, R. L. Siegelman and J. E. Bachman for discussions, and H. Z. H. Jiang for experimental assistance. D.A.R., J.O., J.A.M., D.J.X. and L.E.D. thank the National Science Foundation for graduate fellowship support.

Author Contributions D.A.R., B.K.K. and J.R.L. formulated the project. D.A.R. and B.K.K. synthesized the compounds. D.A.R. and B.K.K. collected and analysed the gas adsorption data. J.O., J.A.M. and T.R. collected and analysed the X-ray diffraction data. D.J.X. collected and analysed the Mössbauer spectra. L.E.D. collected and analysed the magnetic susceptibility data. V.C. and S.B. collected and analysed the infrared spectra. D.A.R., B.K.K. and J.R.L. wrote the paper, and all authors contributed to revising it.

Author Information Reprints and permissions information is available at www.nature.com/reprints. The authors declare competing financial interests: details are available in the online version of the paper. Readers are welcome to comment on the online version of the paper. Publisher's note: Springer Nature remains neutral with regard to jurisdictional claims in published maps and institutional affiliations. Correspondence and requests for materials should be addressed to J.R.L. (jrlong@berkeley.edu).

METHODS

General synthesis and characterization methods. All synthetic procedures were performed under an Ar atmosphere using standard Schlenk techniques or in an N_2-filled VAC Atmospheres glove box. The compound $FeCl_2$ was purchased from Sigma-Aldrich and used as received. Methanol was purchased from EMD Millipore Corporation as DriSolv grade, dried over 3-Å molecular sieves, and sparged with Ar before use. *N*,*N*-dimethylformamide (DMF) was purchased from EMD Millipore Corporation as OmniSolv-grade, sparged with Ar, and dried with an alumina column before use. The linkers H_2bbta (ref. 20) and H_2btdd (ref. 31) were prepared according to previously reported procedures. Ultrahigh-purity-grade (99.999%) He, N_2, H_2 and CO_2, and research-purity-grade (99.99%) CO were used for all gas adsorption measurements and dosing. Elemental analyses for C, H and N were performed at the Microanalytical Laboratory at the University of California, Berkeley.

Synthesis of Fe_2Cl_2(bbta) (1). A solution of $FeCl_2$ (200 mg, 1.58 mmol) and H_2bbta (125 mg, 0.781 mmol) in a mixture of DMF (40 ml) and methanol (10 ml) was added to a Schlenk flash charged with a magnetic stir bar. The solution was stirred at 100 °C for 24 h. The resulting orange powder was collected by filtration, and soaked in 10 ml of DMF at 120 °C for 12 h. The solid was then collected by filtration, and soaked in another 10 ml of DMF at 120 °C for 12 h. This process was repeated five times so that the total time washing with DMF was 3 days. The solid was then collected by filtration, and soaked in 10 ml of methanol at 60 °C for 12 h. The solid was collected by filtration, and soaked in another 10 ml of methanol at 60 °C for 12 h. This process was repeated five times so that the total time washing with methanol was 3 days. The resulting orange solid was collected by filtration, and heated at a rate of 0.2 °C min^{-1} and held at 180 °C under dynamic vacuum for 7 days, affording 200 mg (75%) of product as a yellow powder. Analysis for $C_6H_2Cl_2Fe_2N_6$: calculated: C, 21.15; H, 0.59; N, 24.67; found: C, 20.69; H, 0.61; N, 24.90.

Synthesis of Fe_2Cl_2(btdd) (2). A solution of $FeCl_2$ (200 mg, 1.58 mmol) and H_2btdd (100 mg, 0.376 mmol) in a mixture of DMF (20 ml) and methanol (20 ml) was added to a Schlenk flash charged with a magnetic stir bar. The solution was stirred at 100 °C for 4 days. The resulting brown powder was collected by filtration, and soaked in 10 ml of DMF at 120 °C for 8 h. The supernatant solution was decanted, and 10 ml of DMF was added. This process was repeated once more so that the total time washing with DMF at 120 °C was 1 day. The supernatant solution was decanted, and the solid was soaked in 10 ml of DMF at 140 °C for 8 h. The supernatant solution was decanted, and 10 ml of DMF was added. This process was repeated once more so that the total time washing with DMF at 140 °C was 1 day. The solid was collected by filtration, and soaked in 10 ml of methanol at 60 °C for 8 h. The supernatant solution was decanted, and 10 ml of methanol was added. This process was repeated five times so that the total time washing with methanol was 2 days. The resulting brown solid was collected by filtration, and heated at a rate of 0.2 °C min^{-1} and held at 100 °C under dynamic vacuum for 36 h, affording 140 mg (83%) of product as a brown powder. Analysis for $C_{12}H_4Cl_2Fe_2N_6O_2$: calculated: C, 32.26; H, 0.90; N, 18.81; found: C, 32.51; H, 1.02; N, 18.61.

Gas-adsorption measurements. Gas-adsorption isotherms for pressures of 0–1 bar were measured using a volumetric method using a Micromeritics ASAP2020 or Micromeritics 3Flex gas adsorption analyser. A typical sample of about 100 mg of metal–organic framework was transferred in an N_2-filled glovebox to a pre-weighed analysis tube, which was capped with a Micromeretics TranSeal and evacuated by heating to a specified temperature with a ramp rate of 0.2 °C min^{-1} under dynamic vacuum until an outgas rate of less than 3 μbar min^{-1} was achieved. The evacuated analysis tube containing the degassed sample was then carefully transferred to an electronic balance and weighed again to determine the mass of sample. The tube was then transferred back to the analysis port of the gas adsorption instrument. The outgas rate was again confirmed to be less than 3 μbar min^{-1}. For all isotherms, warm and cold free-space correction measurements were performed using ultrahigh-purity He gas. Isotherms collected at 15–45 °C were measured in water baths using a Julabo F32 water circulator, whereas N_2 isotherms collected at 77 K were measured in liquid-nitrogen baths. Oil-free vacuum pumps and oil-free pressure regulators were used for all measurements to prevent contamination of the samples during the evacuation process or of the feed gases during the isotherm measurements. Langmuir surface areas were determined from N_2 adsorption data collected at 77 K using Micromeritics software.

Powder X-ray diffraction. Microcrystalline powder samples of **1** (about 5 mg) were loaded into two 1.0-mm boron-rich glass capillaries inside a glove box under an N_2 atmosphere. The capillaries were attached to a gas cell, which was connected to the analysis port of a Micromeritics ASAP 2020 gas adsorption instrument. One capillary was fully evacuated at room temperature for 15 min then flame-sealed, while the other capillary was dosed with CO to a pressure of 350 mbar, equilibrated for 2 h, then flame-sealed. Each capillary was placed inside a Kapton tube that was sealed on both ends with epoxy. This process was repeated for samples of **2**, with the exception that CO dosing was performed at a pressure of 700 mbar.

High-resolution synchrotron X-ray powder diffraction data for **1** and CO-dosed **1** were collected at beamline 11-BM at the Advanced Photon Source (APS) at Argonne National Laboratory. Diffraction patterns were collected at 295 K with a wavelength of 0.458996 Å. Discrete detectors covering an angular range from −6° to 16° in 2θ were scanned over a 34° range of 2θ, with data collected every 0.001° and at scan speed of 0.01° s^{-1}. Owing to the large number of data collected, all diffraction patterns were rebinned to a step size of 0.005° in 2θ.

High-resolution synchrotron X-ray powder diffraction data for **2** and CO-dosed **2** were collected at beamline 17-BM at the APS. Diffraction patterns were collected at 298 K with a wavelength of 0.72768 Å. Discrete detectors covering an angular range from −6° to 16° in 2θ were scanned over a 34° range of 2θ, with data collected every 0.001° and at scan speed of 0.01° s^{-1}. Again, all diffraction patterns were rebinned to a step size of 0.005° in 2θ.

For all samples, a standard peak search, followed by indexing via single-value decomposition[32], as implemented in TOPAS-Academic v4.1[33], enables us to determine the approximate unit-cell dimensions. Using TOPAS-Academic, precise unit-cell dimensions were determined by performing a structureless Le Bail refinement, after which Rietveld refinements were performed. For **2** and CO-dosed **2**, a structural model constructed in Materials Studio (Materials Studio v5.0.0.0, 2009, Accelrys Software Inc.) was used in the Rietveld refinement, as described in the Supplementary Information.

For *in situ* powder X-ray diffraction measurements of **1**, a microcrystalline powder sample (about 5 mg) was loaded into a 1.0-mm glass capillary inside a glove box under an N_2 atmosphere. The capillary was attached to a gas cell, which was connected to the analysis port of a Micromeritics ASAP 2020 gas adsorption instrument and then evacuated. It was then dosed with CO to a pressure of 300 mbar, equilibrated for 2 h, and flame-sealed. High-resolution synchrotron X-ray powder diffraction data were subsequently collected at beamline 17-BM at the APS. Diffraction patterns were collected at various temperatures with a wavelength of 0.72768 Å. During the course of the experiment, the temperature was cycled between 273 K and 353 K at rates varying from 3 K min^{-1} to 6 K min^{-1}. In total, four cycles were performed with patterns collected every minute. Qualitative phase data were obtained using simultaneous sequential Rietveld refinements.

Infrared spectroscopy. Fourier transform infrared (FTIR) spectra were collected in transmission mode on a self-supported wafer of sample, in a controlled atmosphere using a custom-built infrared cell. The spectra were recorded at 2-cm^{-1} resolution on a Bruker IFS 66 FTIR spectrometer, equipped with a MCT detector. Spectra were collected during adsorption and desorption of CO at 25 °C. Before CO was exposed to the sample, the sample was first activated at 150 °C for 15 min while flowing 30 ml min^{-1} of pure N_2 (heating ramp rate of 1 °C min^{-1}).

Mössbauer spectroscopy. Mössbauer spectra were measured at 100 K with a constant-acceleration spectrometer, which used a rhodium-matrix cobalt-57 source. Isomer shifts are reported relative to 27-μm α-iron foil at 295 K. The absorber contained about 40 mg cm^{-2} of powdered sample. The CO-loaded sample was prepared by attaching a glass tube containing activated **1** to a Micromeritics ASAP 2020 surface area and porosity analyser, dosing with 1 bar of CO at 295 K, and allowing the sample to equilibrate for 1 h. The sample was then cooled to 77 K and evacuated, and immediately transferred to the spectrometer.

Measurements of d.c. magnetic susceptibility. Samples were prepared by adding crystalline powder (14 mg for **1**, 28 mg for **1**·2CO) to a 5-mm-inner-diameter quartz tube containing a raised quartz platform. Sample powders were restrained with a plug of compacted glass wool that prevented crystallite torqueing, but enabled gas-dosing with CO. The CO-loaded samples were prepared by attaching the quartz tubes containing activated **1** to a Micromeritics ASAP 2020 gas adsorption analyser. Adsorption isotherms were then collected until the pressure of the atmosphere of CO gas in the sample tubes reached 300 mbar of CO, at which point the measurements were terminated. The quartz tubes were then cooled in liquid N_2 and flame-sealed. Magnetic susceptibility measurements were performed using a Quantum Design MPMS2 SQUID magnetometer. Measurements of d.c. magnetic susceptibility were collected in the temperature range 2–300 K under applied magnetic fields of 1 T. Diamagnetic corrections were applied to the data using Pascal's constants to give $\chi_D = -0.00014752$ emu mol^{-1} for **1** and $\chi_D = -0.00016872$ emu mol^{-1} for **1**·2CO.

Differential scanning calorimetry. Heat-capacity measurements were collected on a TA Instruments Q200 differential scanning calorimeter (DSC) equipped with refrigerated cooling system RSC90 under a He flow. Baseline data for the empty heating chamber were collected between the temperatures of −90 °C and 400 °C, followed by a temperature calibration using the melting point of an indium sample. A sample of **1** (5.5 mg) was hermetically sealed in an aluminium pan under an N_2 atmosphere. The heat-flow data were collected by using a modulated DSC program with a temperature ramp rate of 2 °C min^{-1} in the temperature range of −20 °C to 150 °C, using a temperature modulation of ±0.75 °C per 80 s using a standard modulated DSC method and TA Instruments software.

Data availability. The main data supporting the findings of this study are available within the paper and its Supplementary Information. Extra data are available from the corresponding author on request. Metrical data for the solid-state structures of Fe_2Cl_2(bbta), CO-dosed Fe_2Cl_2(bbta), Fe_2Cl_2(btdd) and CO-dosed Fe_2Cl_2(btdd) are available free of charge from the Cambridge Crystallographic Data Centre under reference numbers 1571058–1571061.

31. Denysenko, D. *et al.* Elucidating gating effects for hydrogen sorption in MFU-4-type triazolate-based metal–organic frameworks featuring different pore sizes. *Chem. Eur. J.* **17,** 1837–1848 (2011).
32. Coelho, A. A. Indexing of powder diffraction patterns by iterative use of singular value decomposition. *J. Appl. Cryst.* **36,** 86–95 (2003).
33. Coelho, A. A. TOPAS-Academic, version 4.1 (Coelho Software, 2007).